Chapter 4

Linear Theory

4.1 INTRODUCTION

The linear theory relating interval slowness to stacking slowness plays a central role in the velocity-analysis algorithm proposed in this thesis. Lynn (1980) first derived a linear operator that related laterally varying components of interval slowness to the corresponding, laterally varying components of stacking slowness. His theory required that the interval slowness be constant in depth. Then, Loinger (1983) proposed a more detailed linear theory that allowed the interval slowness distribution to vary in depth. His derivation was based on flat reflectors and a constant background slowness.

The linearization presented here is similar to that of Loinger. Indeed, for the case of flat reflectors and a constant background-slowness, it differs only in a few details. The derivation presented here does, however, allow for more general models. In addition to the linear theory based on flat dips and constant background-slowness, two generalizations are presented. The first is valid for flat dips and a depth-variable background-slowness; the second requires a constant background-slowness, but allows for dipping reflectors.

This chapter begins with a detailed derivation of this theory, then continues with a discussion of the properties of the derived linear operator. It concludes with a synthetic data example, in which the linear operator is applied in two ways: first, as a forward operator to calculate the stacking slownesses due to a synthetic interval-slowness model; second, as an inverse operator to calculate the interval-slowness model from the stacking slownesses derived through ray tracing.

4.2 DERIVATION OF LINEAR THEORY: GENERAL FORMULATION

The linearization of the relationship between interval slowness and stacking slowness depends on a proper interpretation of stacking slowness: it is a parameter that describes a hyperbola over offset and time. According to this interpretation, the stacking slowness corresponding to an assumed interval-slowness model must be calculated through the intermediary of the traveltimes. That is, corresponding to an assumed interval-slowness model will be a set of traveltimes. For each reflector and midpoint, these traveltimes can be fit over offset with a hyperbola. The parameter describing that hyperbola is the stacking slowness for that midpoint and reflector.

This relationship between interval slowness, traveltime, and stacking slowness can be more clearly understood if the traveltimes t corresponding to the different offsets x are considered in x^2–t^2 space. Then, the hyperbola becomes a straight line, whose slope is the square of the stacking slowness. That is, the hyperbola in x and t described by the NMO equation

$$t^2 = \tau^2 + x^2 w_s^2,$$

is a straight line with slope w_s^2 in x^2–t^2 space.

The calculation of the stacking slowness for one midpoint and reflector, corresponding to an interval-slowness model then takes the following simple form. Find the slope of the best-fit line to the set of points x_j^2, $t_j^2(w_{in})$, where $t_j(w_{in})$ is the traveltime for offset x_j, as calculated from the interval slownesses w_{in}. This calculation is given by a standard result from least-squares analysis:

$$w_s^2 = \frac{\sum_{j=1}^{n} \left(x_j^2 - \overline{x^2} \right) t_j^2(w_{in})}{\sum_{j=1}^{n} \left(x_j^2 - \overline{x^2} \right)^2} . \tag{4.1}$$

The sums in equation (4.1) range over offset, where n is the number of offsets. $\overline{x^2}$ is the mean squared offset. Thus, as shown in equation (4.1), stacking slowness depends on traveltime, which in turn depends on interval slowness.

Part 1: Δw_s due to Δt

Suppose that the interval slownesses are changed by a small amount. This will change each traveltime from t_j to $t_j + \Delta t_j$. Then, according to equation (4.1), the stacking slowness for this midpoint gather and reflector will change to

$$(w_s + \Delta w_s)^2 = \frac{\sum_{j=1}^{n} \left(x_j^2 - \overline{x^2} \right) (t_j + \Delta t_j)^2}{\sum_{j=1}^{n} \left(x_j^2 - \overline{x^2} \right)^2} . \tag{4.2}$$

Assuming that the change in traveltime is small, the resulting change in stacking slowness will be

$$\Delta w_s = \frac{1}{w_s} \frac{\sum_{j=1}^{n} \left(x_j^2 - \overline{x^2} \right) t_j \, \Delta t_j}{\sum_{j=1}^{n} \left(x_j^2 - \overline{x^2} \right)^2} . \tag{4.3}$$

Equation (4.3) expresses the change in stacking slowness due to a change in traveltime as a weighted sum over offset of the traveltime perturbations, Δt_j. The meaning of the offset-dependent weights is shown in Figure 4.1. Increasing the traveltime at a small offset will decrease the slope of the line; at a large offset, the same increase in traveltime will increase the slope.

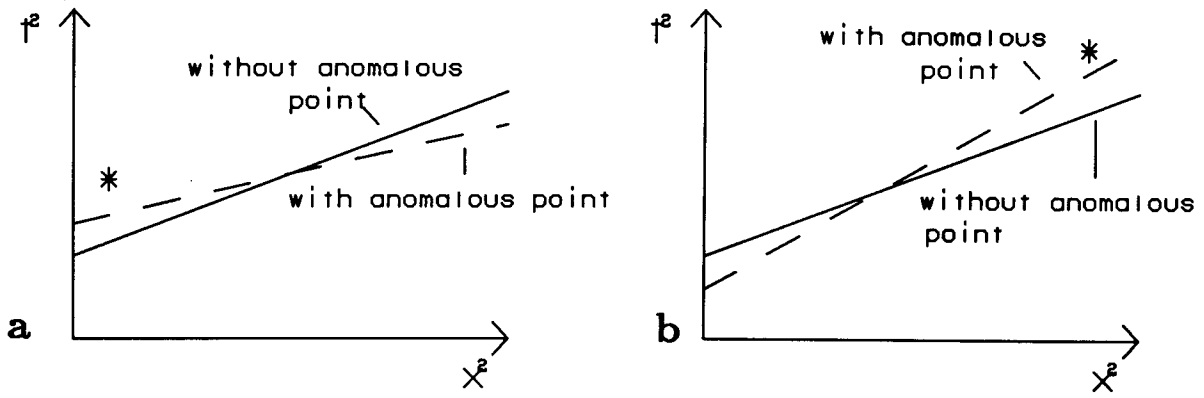

FIG. 4.1. a) $t^2 - x^2$ plot with increased traveltime for one trace at small offset. b) $t^2 - x^2$ plot with increased traveltime for one trace at large offset.

The size of the weights depends on the recording geometry. In calculating these weights, appendix A shows that they depend on the range of offset values. Under the assumption that the minimum offset, x_0, is zero, Appendix A shows that equation (4.3) can be explicitly written as

$$\Delta w_s = \frac{1}{w_s} \frac{\sum_{j=1}^{n} \left(x_j^2 - \frac{L^2}{3} \right) t_j \, \Delta t_j}{\frac{4}{45} n L^4} . \tag{4.4}$$

In equation (4.4), L is the maximum offset (called the *cable length* throughout this thesis). Because common recording geometries have a minimum offset that is several times larger than the regular offset increment, the derivation in Appendix A also leads to the analog of equation (4.4) for the general case of $x_0 \neq 0$ (see equation A.9).

Part 2: Δt due to Δw_{in}

Thus far, the linearization has focussed on the relationship between traveltime and stacking slowness. That is, equation (4.4) requires only that t_j and Δt_j be provided; it is insensitive to how they are calculated. This calculation is described by the second part of the linearization, which relates a change in interval slowness to the corresponding change in traveltime.

As is well known in seismic tomography (Aki and Richards, 1980, Fawcett, 1983), this change is easily calculated with the help of Fermat's principle. The j^{th} component of the traveltime (j refers to a specific reflector, offset and midpoint) can be written as

$$t_j = \int_{S_j} w_{in}(y_a, z_a)\, dS_j \ , \tag{4.5}$$

where S_j is the j^{th} raypath. $w_{in}(y_a, z_a)$ is the interval slowness at depth z_a and midpoint y_a. Because the raypath depends on the interval slownesses, t_j is a non-linear function of w_{in}.

If the interval slowness changes to $w_{in}'(y_a, z_a) = w_{in}(y_a, z_a) + \Delta w_{in}(y_a, z_a)$, the approximate change in the traveltime will be:

$$\Delta t_j = \int_{S_j} \Delta w_{in}(y_a, z_a)\, dS_j \ . \tag{4.6}$$

Equation (4.6) says that the change in traveltime is just the integral along the *unperturbed* ray S_j, through the anomalous interval slowness distribution $\Delta w_{in}(y_a, z_a)$.

Part 3: Δw_s due to Δw_{in}

With the expressions for t_j and Δt_j given by equations (4.5) and (4.6), equation (4.4) could be used directly to calculate the change in stacking slowness due to a change in interval slowness. This calculation would proceed as follows. First, calculate the stacking slowness, w_s, and traveltimes, t_j, corresponding to the original set of interval slownesses (the so-called background model). Then, calculate the change in traveltime, Δt_j, due to the change in interval slowness. Finally, form a weighted sum of these Δt_j according to equation (4.4). The calculation could then be repeated for all midpoints and reflectors of interest.

Although this form of the calculation is valid for any type of interval-slowness model, it does not offer any insight into the general properties of the relationship between interval slowness and stacking slowness. The stacking-slowness response to an impulse of anomalous interval slowness can be derived through a reorganization of the calculation. A study of this impulse response, and its associated transfer function, will lead to considerable insight into the general nature of the linear theory relating interval slowness perturbations to stacking-slowness perturbations.

4.3 DERIVATION OF THE IMPULSE RESPONSE, $G(y, z_r, y_a, z_a)$

The impulse response $G(y, z_r, y_a, z_a)$ relates a perturbation in the interval slowness at (y_a, z_a) to the resulting stacking-slowness perturbation at (y, z_r). That is, the change in stacking slowness for midpoint y, for the reflector at depth z_r, will be written as

$$\Delta w_s(y, z_r) = \int_{y_a} \int_{z_a} G(y, z_r, y_a, z_a)\, \Delta w_{in}(y_a, z_a)\, dz_a\, dy_a \quad . \tag{4.7}$$

Equation (4.7) calculates $\Delta w_s(y, z_r)$ by integrating over the "fan" of Figure 4.2. The value of the impulse response, $G(y, z_r, y_a, z_a)$, depends on the offset of the ray that goes through the point (y_a, z_a) for this y and z_r. That is, the response depends on the location of (y_a, z_a) within the "fan" for this y and z_r. For a different midpoint, the anomaly at (y_a, z_a) would be seen by a ray at a different offset, and therefore the response would also be different.

For a given midpoint gather and reflector, the impulse response depends on the offset of the ray that goes through the point (y_a, z_a). On the other hand, ray tracing provides the coordinates of a ray for a given offset, midpoint and reflector. Thus, the raypath information must be reorganized for the calculation of the impulse response. In general, one could construct a table of raypath coordinates, then for each midpoint and reflector, find the offset of the ray that goes through (y_a, z_a) by looking it up in the table.

For the flat reflectors and constant background slowness of figure 4.2, the process is even simpler: for each midpoint and reflector, calculate analytically the offset of the ray that goes through the point y_a, z_a. The derivation of the impulse response then takes the following form. First, with the help of a delta function that rides along the ray, the calculation of the traveltime perturbation can be changed from an integration along the raypath to an integration over the entire model. Then, as the sum runs over offset in equation (4.4), only the contribution of the ray that goes through (y_a, z_a) will be non-

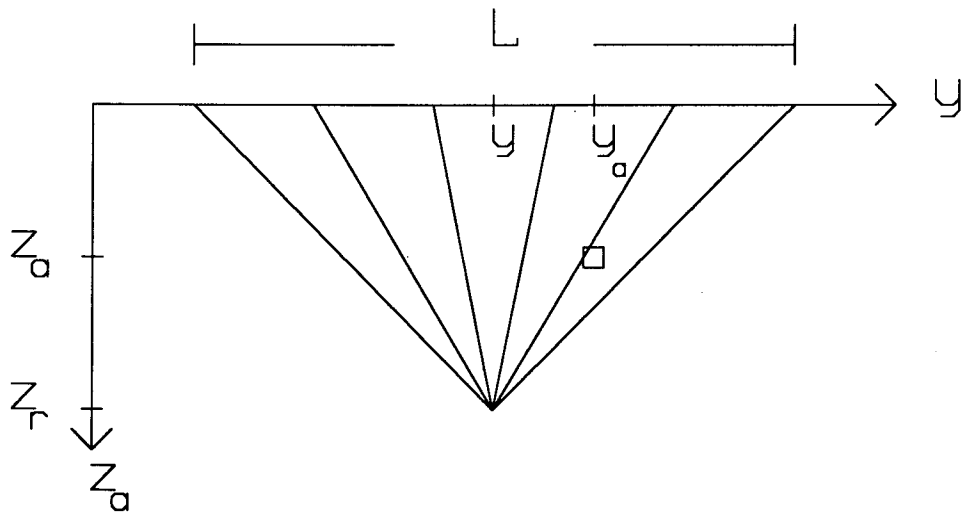

FIG. 4.2. Geometry for a constant background-slowness and a flat reflector. Shown are a few raypaths to the reflector at depth z_r for the midpoint gather at y. The maximum offset is L. The impulse of anomalous interval slowness has coordinates y_a, z_a.

zero. The result will be the stacking slowness response at midpoint y and reflector z_r, to the impulse of anomalous interval slowness at (y_a, z_a).

Figure 4.3 shows the raypath to a flat reflector at depth z_r, for the offset x and midpoint y. When the ray with offset x has reached depth z_a, its horizontal distance from the midpoint y is defined in figure 4.3 to be μ_x. Note that μ_x has two possible values, one for the downgoing path and one for the upgoing path. Thus, equation (4.6) can be rewritten as

$$\Delta t_x = \int_{y_a}\int_{z_a} \Delta w_{in}(y_a, z_a)\left(\frac{\delta\left[y_a - y - \mu_x(z_a)\right] + \delta\left[y_a - y + \mu_x(z_a)\right]}{\cos\theta_x}\right) dy_a\, dz_a \quad . \quad (4.8)$$

The subscript x specifies the offset of the ray in question. Because only one particular midpoint gather and reflector are being considered at this point of the derivation, specifying the offset is equivalent to specifying the ray.

If Δt_x given by equation (4.8) is now substituted into equation (4.4), and the integrals over the model (i.e. over y_a and z_a) are pulled outside the sum over offset, the result is

$$\Delta w_s = \int_{y_a}\int_{z_a} G(y_a, z_a)\, \Delta w_{in}(y_a, z_a) dy_a\, dz_a \quad , \quad (4.9)$$

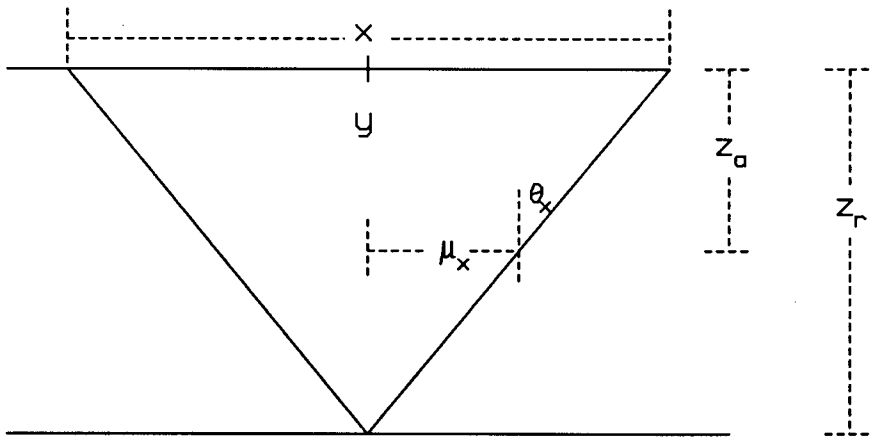

FIG. 4.3. Raypath to a flat reflector at depth z_r, for the offset x and midpoint y. The background model has constant interval slowness. When the ray has reached depth z_a, its horizontal distance from the midpoint y is given by μ_x. θ_x is the angle that this ray makes with the vertical.

where

$$G(y_a, z_a) = \frac{45}{4nL^4}\sum_x \left(x^2 - \frac{L^2}{3} \right) \frac{t_x}{w_s} \times \left(\frac{\delta\left[y_a - y - \mu_x(z_a)\right] + \delta\left[y_a - y - \mu_x(z_a)\right]}{\cos\theta_x} \right). \tag{4.10}$$

Equation (4.9) thus expresses the stacking-slowness perturbation for a particular midpoint and reflector, as a weighted sum (integral) of interval-slowness perturbations. Equation (4.10) specifies the weight, or impulse response. All that remains is the calculation of the impulse response in equation (4.10).

If the offset increment is assumed to be small, $1/n \approx dx/L$, and the sum in equation (4.10) can be converted to an integral:

$$G(y_a, z_a) = \frac{45}{4L^5}\int_{x=0}^{x=L} \left(x^2 - \frac{L^2}{3} \right) \frac{t_x}{w_s} \times \left(\frac{\delta\left[y_a - y + \mu_x(z_a)\right] + \delta\left[y_a - y - \mu_x(z_a)\right]}{\cos\theta_x} \right) dx . \tag{4.11}$$

The background model of figure 4.3 allows several simplifications of equation (4.11). The unperturbed stacking slowness, w_s, is equal to the background slowness w. Then the unperturbed traveltime is given by the NMO equation:

$$t_x = w\left(x^2 + 4z_r^2\right)^{1/2} . \tag{4.12}$$

Furthermore, the propagation angle depends only on the offset and depth to reflector:

$$\cos\theta_x = \frac{2z_r}{\left(x^2 + 4z_r^2\right)^{1/2}} . \tag{4.13}$$

Finally, Figure 4.3 shows that

$$\mu_x(z_a) = \frac{x}{2}\left(\frac{z_r - z_a}{z_r}\right) . \tag{4.14}$$

If this μ is used in the delta functions of equation (4.11), the result is

$$\delta\left[y_a - y \pm \mu_x(z_a)\right] = \delta\left[y_a - y \pm \frac{x}{2}\left(\frac{z_r - z_a}{z_r}\right)\right] . \tag{4.15}$$

A standard identity for delta functions (Bracewell, 1965) allows equation (4.15) to be rewritten as

$$\delta\left[y_a - y \pm \mu_x(z_a)\right] = \frac{\delta\left[2\left(y_a - y\right)\left(\frac{z_r}{z_r - z_a}\right) \pm x\right]}{\left[\frac{z_r - z_a}{2z_r}\right]} . \tag{4.16}$$

Equation (4.16) can be further simplified with the definition of the *effective cable length*, L' :

$$L' = \left(\frac{z_r - z_a}{z_r}\right) L .$$

As can be seen in Figure 4.4, of the anomalies at depth z_a, those within L' of the midpoint y will affect the stacking slowness at midpoint y and reflector z_r. L' is thus the aperture of the filter at depth z_a, for the reflector at depth z_r.
Equation (4.16) can thus be written as

$$\delta\left[y_a - y \pm \mu_x(z_a)\right] = \frac{\delta\left[2\left(y_a - y\right)\left(\frac{L}{L'}\right) \pm x\right]}{\left[\frac{L'}{2L}\right]} . \tag{4.17}$$

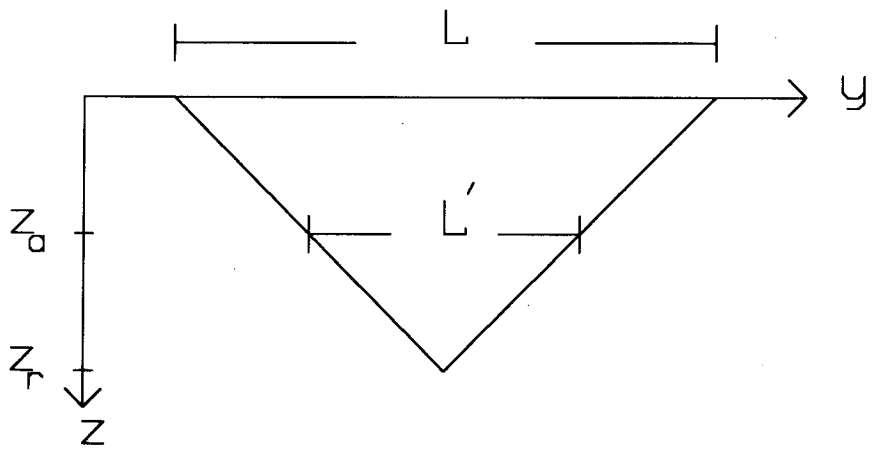

FIG. 4.4. L is the maximum offset, i.e. the cable length. L' is the effective cable length for the reflector at depth z_r and an anomaly at depth z_a. Anomalies within $L'/2$ to either side of the midpoint y will affect the stacking slowness at midpoint y and reflector at z_r.

With the substitution of equations (4.12), (4,13) and (4.17) into equation (4.11), the derivation is complete. That is, with the help of the delta function of equation (4.17), the integral over x of equation (4.11) just selects the ray with $x = 2\left|y_a - y\right|(L/L')$.

Finally then, the response at midpoint y, for the reflector at depth z_r, to an impulse of anomalous interval slowness at (y_a, z_a), is

$$G(y, z_r, y_a, z_a) = \frac{15 z_r}{L^2 L'}\left[3\left(\frac{2(y_a - y)}{L'}\right)^2 - 1\right]\left[1 + \frac{L^2}{4 z_r^2}\left(\frac{2(y_a - y)}{L'}\right)^2\right] \qquad (4.18)$$

$$\text{for } \left|y_a - y\right| < \frac{L'}{2}.$$

$$= 0 \quad \text{for } \left|y_a - y\right| > \frac{L'}{2}.$$

Under the assumption that $L \ll z_r$, equation (4.18) reduces to the result derived by Loinger (1983):

$$G(y, z_r, y_a, z_a) = \frac{15 z_r}{L^2 L'}\left[3\left(\frac{2(y_a - y)}{L'}\right)^2 - 1\right] \quad \text{for } \left|y_a - y\right| < \frac{L'}{2} \qquad (4.19)$$

$$= 0 \quad \text{for} \left| y_a - y \right| > \frac{L'}{2}$$

The derivation of this section was based on flat reflectors and a constant background-slowness. Because the largest variation in velocity in the earth is usually in the depth direction, a depth-variable background-slowness is more appropriate. Appendix B presents a full development of the linearization for a depth-variable background and flat reflectors.

Although the linear equation derived in Appendix B requires the numerical evaluation of the integral over offset, an approximate result is extremely similar to equation (4.18). As shown in Appendix B, equation (4.18) is approximately valid for a depth-variable background, provided that the correct values for the effective cable length, L', are used. As shown in Figure 4.5, these correct values are the coordinates of the far-offset ray for the given reflector. Thus, implementing equation (4.18) for a depth-variable background requires that one ray be traced for each reflector, so that the set of values $L'(z_a, z_r)$ could be built.

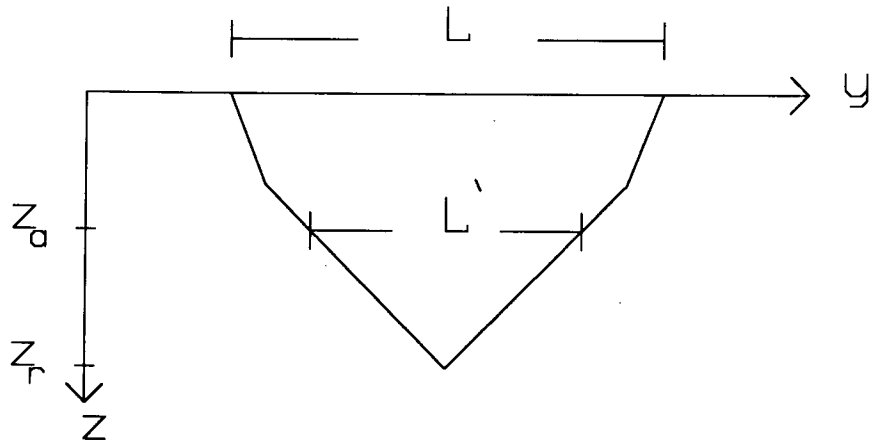

FIG. 4.5. Effective cable length for a background slowness that varies with depth.

4.4 DISCUSSION OF LINEAR OPERATOR

The impulse response G in equation (4.18) depends only on the difference $y - y_a$: the integral over midpoint y_a in equation (4.9) is a convolution. This convolutional form is due to the laterally invariant background-slowness and the flat reflector. The impulse response is shown in Figure 4.6. The range of influence of a point anomaly depends on how its depth relates to the depth of the reflector. Thus, the width of the response is L' .

Further insight into the nature of this impulse response can be gained by a look at its Fourier transform. Thus, transforming the impulse response $G(y, z_r, z_a)$ over y to $\overline{G}(K, z_r z_a)$, then using a dimensionless wavenumber $k = \frac{KL}{2}\frac{(z_r - z_a)}{z_r} = \frac{KL'}{2}$, gives the following transfer function:

$$\overline{G}(k, z_r, z_a) = \frac{15 z_r}{L^2 k^5}\left[\left((2+2c)k^4 - (34c+6)k^2 + 72c\right)\sin k + \left((6+10c)k^3 - 72ck\right)\cos k\right] \tag{4.20}$$

where $c = \frac{L^2}{4z^2}$, the normalized cable length. This transfer function is plotted in figure 4.7 for $c = .4$. For $c = 0$, and k small, the transfer function is $\approx -k^2$, that is, a second derivative operator over midpoint. A similar result was derived and discussed by Lynn and Claerbout (1982).

The first thing to notice in Figure 4.7 is that the transfer function is not equal to zero at $k = 0$; in particular it is positive. This is an intuitively satisfying result, since it says that an increase in the DC component of interval slowness will produce an increase in the DC component of stacking slowness.

Another interesting feature that can be seen in Figure 4.7, is that the magnitude of the transfer function achieves a maximum at $k \approx 3.5$. This feature can be thought of as a resonance phenomenon, since for a given depth of reflector, depth of anomaly and cable length, there is a particular wavelength of interval slowness anomaly that will produce a maximum in the stacking slowness response. More quantitatively, the resonance occurs at $k = \frac{KL'}{2} \approx 3.5$, that is, when the wavelength of the anomaly, λ, is approximately equal to the effective cable length, L' .

Figures 4.8 and 4.9 provide an explanation for the resonance. Figure 4.8 shows a wavelength of interval slowness anomaly, λ, equal to the effective cable length L' . If the small offsets sense a negative slowness anomaly, then the large offsets will sense a

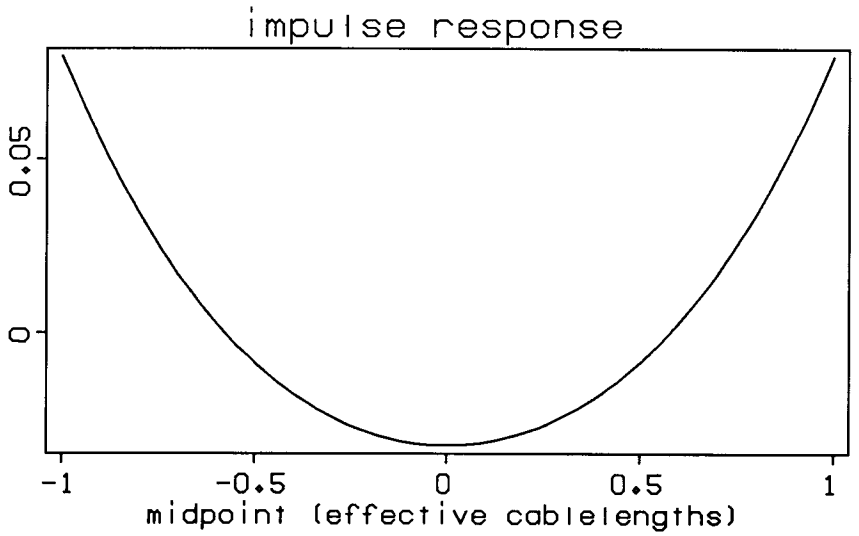

FIG. 4.6. Stacking slowness response as a function of midpoint, to an impulse of interval slowness. The range of influence of a point anomaly depends on how its depth z_a is related to the depth of the reflector z_r. Thus, the stacking slowness at midpoints within an effective cable length $L' = L\,(z_r - z_a)/z_r$ of the impulse of interval slowness will be changed.

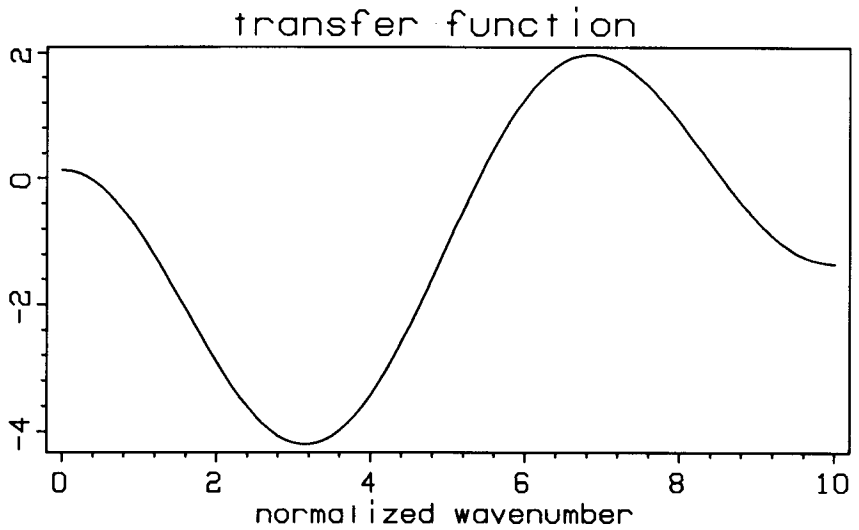

FIG. 4.7. Transfer function versus normalized wavenumber k. The wavenumber has been normalized by the effective cable length, L'. Note the large negative response at $k = 3.5$, or $\lambda \approx L'$

positive anomaly (see figure 4.8).

Figure 4.9 shows the corresponding traveltime picture: the small offsets have their traveltimes decreased due to the anomalously small slowness (high velocity) that they sense, while the large offsets have their traveltimes increased due to the anomalously large slowness (low velocity) that they sense. The near and far offsets are thus reinforcing one another to produce a maximum change in the slope of the best fit line, that is, the stacking slowness. Note from figure 4.9 that the slope of the line increases when the midpoint sits above a negative slowness anomaly. Thus the response is negative at the resonant wavenumber.

4.5 EIGENVECTORS AND EIGENVALUES

The analysis of the previous section showed how the interval slownesses at a particular depth affect the stacking slowness. This section takes the next step, and looks at how different components of an entire interval-slowness model affect the stacking slowness. Because the theory is linear, an eigenvector analysis is an appropriate way to study which components of the model are well determined, and which are poorly determined. This section performs this eigenvector analysis on a discrete version of equation (4.7), by means of a singular value decomposition (SVD).

The anomalous interval slowness model can be expressed in terms of a set of n basis functions $h_j(y_a, z_a)$.

$$\Delta w_{in}(y_a, z_a) = \sum_{j=0}^{n} m_j h_j(y_a, z_a) . \tag{4.21}$$

The m_j are the expansion coefficients.

Inserting equation (4.21) into equation (4.7) converts the integral of equation (4.7) into a sum,

$$[\Delta w_s]_i = \sum_{j=0}^{n} G_{ij} m_j , \tag{4.22}$$

where

$$G_{ij} = \int_{z_a}\int_{y_a} G(z_r, y, y_a, z_a) h_j(y_a, z_a) dz_a \, dy_a . \tag{4.23}$$

The subscript i refers to the point in the data space: each $[\Delta w_s]_i$ is the anomalous stacking slowness for a specific reflector at a specific midpoint. Throughout this thesis, I use basis functions that are sines and cosines in the midpoint direction, and thin strips in depth. Figure 4.10 shows one such basis function.

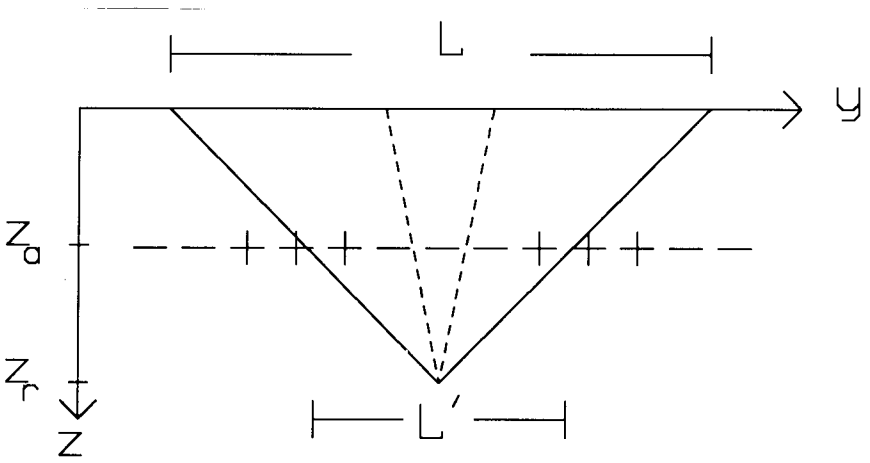

FIG. 4.8. Anomaly at depth z_a with wavelength equal to the effective cable length ($\lambda = L'$). The small offsets sense a negative slowness anomaly, the large offsets a positive anomaly.

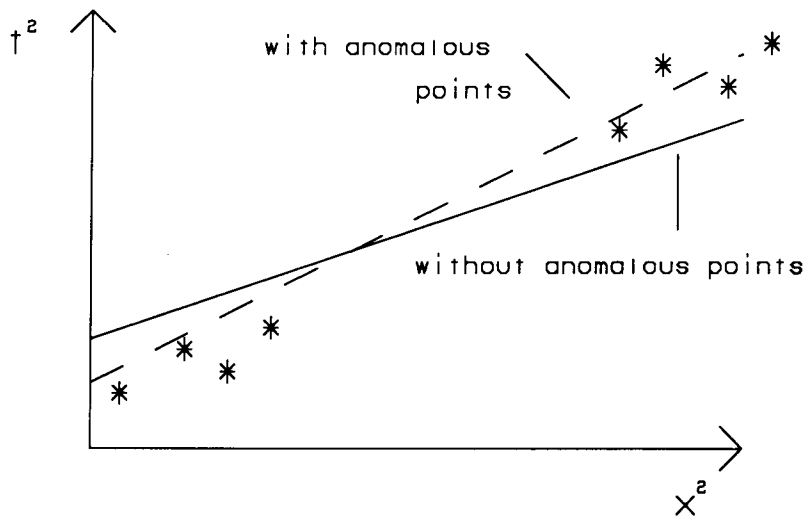

FIG. 4.9. Traveltimes corresponding to figure 4.8. Due to the anomaly, the traveltimes for the small offsets have decreased, those at large offsets have increased. Thus the slope of the best fit line, the square of the stacking slowness $w_s{}^2$ is increased. Furthermore, the increase is large because the effects of the small and large offsets reinforce one another.

For the purposes of this study, the model consisted of 10 layers, with one reflector at the bottom of the model. The full set of parameters are the following:

depth of reflector = 1650 m
width of model = 7900 m
cable length = 1600 m
maximum k_y = 24 → shortest wavelength = 330 m
number of anomalous depths = 10, each of thickness 165 m.
stacking slownesses recorded at 64 midpoints

For these parameters, a vector in the data space has 64 elements. A model-space vector has (2 ×24^-^1)×10 = 470 elements, one for each basis function. The factor of 2 enters because each frequency has a basis function that is a sine, and one that is a cosine. Thus, the dimensions of the matrix **G** are 64 by 470.

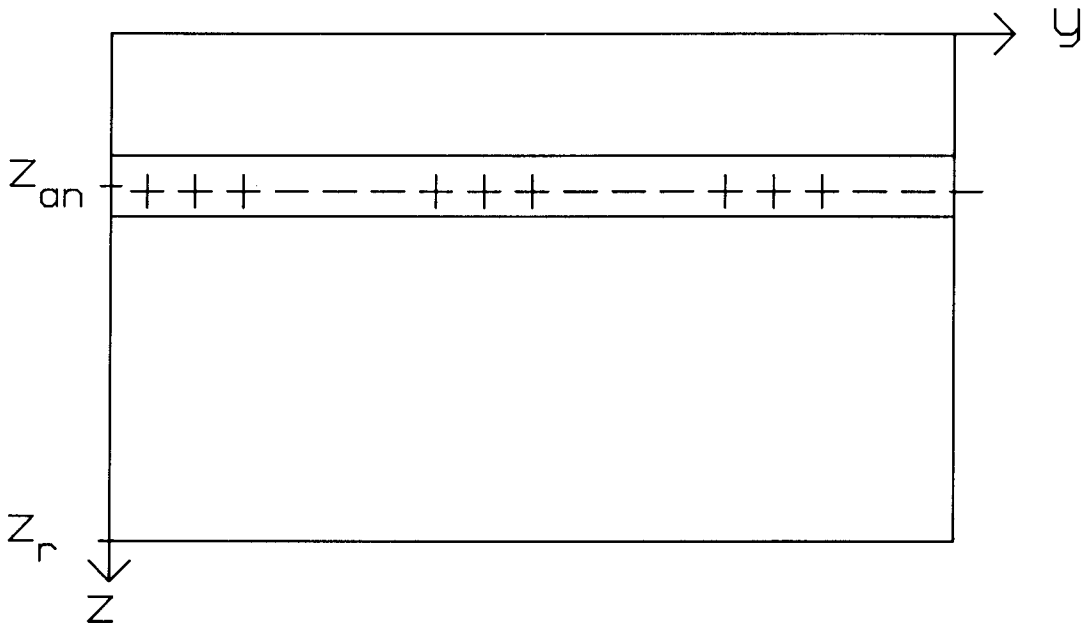

FIG. 4.10. Basis function at depth z_a and thickness Δz_a. In the lateral direction it is a sine with period equal to 1/3 the width of the model.

Eigenvectors

The resolution of a particular component of the interval velocity model is related to how strongly that component affects the data. Components which have little or no effect on the data will be poorly resolved, whereas those which most affect the data will be best resolved. The singular value decomposition (SVD) of **G** (see Strang, 1980, Aki

and Richards, 1980) is particularly useful in the study of resolution, because it allows one to directly examine how well each component of the model can be determined.

The singular value decomposition of the matrix **G** leads to:

$$\mathbf{G} = \mathbf{U}\Lambda\mathbf{V} \tag{4.24}$$

where **U** is the matrix of data-space eigenvectors, **V** the matrix of model-space eigenvectors, and Λ a matrix with entries (the eigenvalues) along the diagonal. Shown in Figure 4.11 are two of the model-space eigenvectors. Because G in equation (4.23) depends only on the distance of the midpoint y from the anomaly at y_a, it is not surprising that the eigenvectors are laterally sinusoidal. At the right of figure 4.11 is a vertical slice through each eigenvector. The vertical slices emphasizes the amplitude as a function of depth.

The amplitude distribution shown in the vertical slices can be best understood with the help of the transfer function, which is shown again in figure 4.12. The horizontal scale is the midpoint wavenumber axis, normalized in such a way that the units are wavelengths of anomaly per effective cable length. For example, the response at $k = 1$ is the stacking slowness response to an interval slowness anomaly with wavelength equal to the effective cable length.

Suppose that the wavelength of the anomaly in the earth is fixed at a particular value, say 1 cable length. The response to an anomaly at the surface with wavelength equal to one cable length will be –4 (i.e. the response at $k = 1$). Then as the depth of the anomaly increases, the effective cable length decreases. The corresponding response can be found by moving back along the k axis (towards the origin) an appropriate amount. As the depth of anomaly approaches the depth of the reflector, the response will approach the response at $k = 0$. This is due to the fact that when the effective cable length gets very small, the normalized wavenumber of any anomaly appears to be very small.

Now return to the vertical slices of figure 4.11. Each of these curves is just the appropriate portion of the transfer function: each one starts at the surface with a response determined by the number of wavelengths per actual cable length, then as the depth increases, the response moves towards the zero-wavenumber, i.e. DC, response. Because the eigenvectors of Figure 4.11 have been normalized, the actual value of the response shown in Figure 4.11 differs from that shown in Figure 4.12. The relative values correspond exactly to figure 4.12.

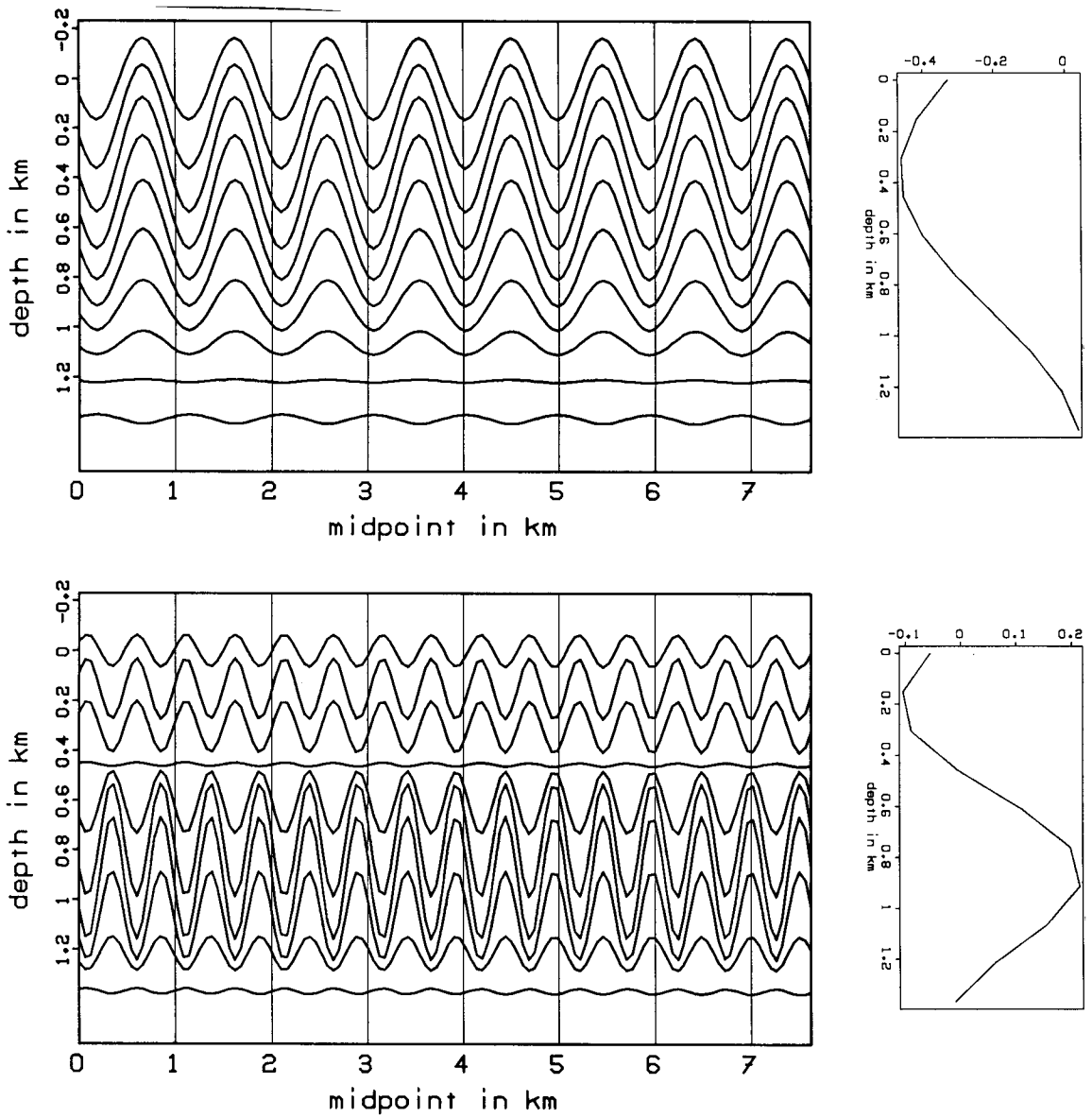

FIG. 4.11. Model-space eigenvectors. Each one is a sinusoid laterally, with the vertical distribution of amplitude shown at right.

Eigenvalues

The magnitude of the eigenvalue associated with each of the eigenvectors described in the last section is a measure of how strongly that component affects the data. Because the smaller dimension of the matrix **G** in equation (4.24) is 64, one would expect at most 64 non-zero eigenvalues.

Figure 4.13 shows the eigenvalues, plotted in order of decreasing size. Because the sine and the cosine of each wavelength are equally well determined, the eigenvalues come in pairs. Note that there are only 47 non-zero values, corresponding to the 47 sines and

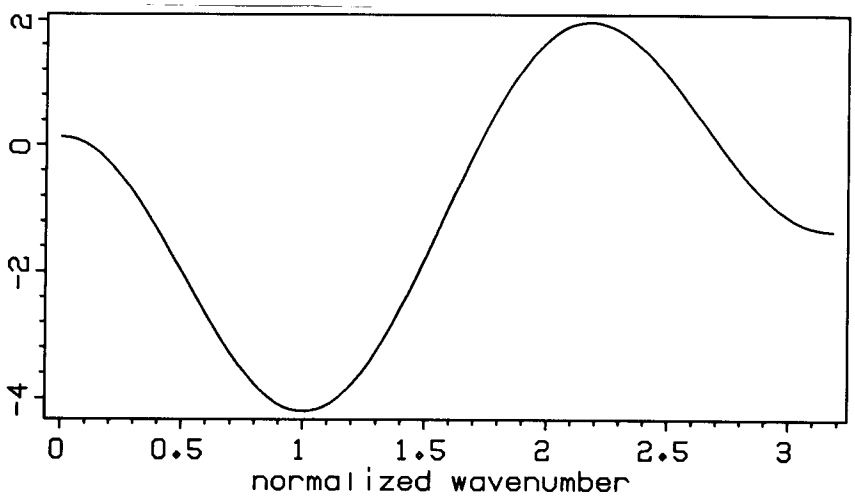

FIG. 4.12. Transfer function. The horizontal coordinate has been normalized in such a way that the scale now refers to the number of wavelengths per effective cable length.

cosines. This limitation occurs because the data space can only contain components that are linear combinations of the sines and cosines.

An even more revealing way to look at the eigenvalues is to plot eigenvalue versus wavenumber of the corresponding eigenvector. Figure 4.14 makes this comparison. It shows that the response is fairly flat for the higher wavenumbers, but drops off sharply for the low wavenumbers.

In particular, the three lowest wavenumbers all have eigenvalue of about 1—a factor of 10 less than most of the others. The eigenvector with the lowest eigenvalue, is the DC, or zero-frequency component. The next two have wavelengths equal to the width of the entire model and half the model respectively. The width of the model is about 6 cable lengths. Thus all three of these poorly determined components have wavelengths of 3 cable lengths or more.

This result was to be expected from the earlier discussion of the transfer function. Not only is there a zero in the response at a normalized wavenumber of .1, but the entire response from about .2 back to the origin is weak (see Figure 4.12). Thus all wavelengths of about 5 effective cable lengths or greater are weakly determined. The component with wavelength equal to 3 cable lengths has, over most of its depth range, an effective cable length of 5 or greater, and is therefore weakly determined. The linear filter that is examined here is like a second derivative operator with a small DC component added in (see figure 4.6). The very long wavelength anomalies appear to be

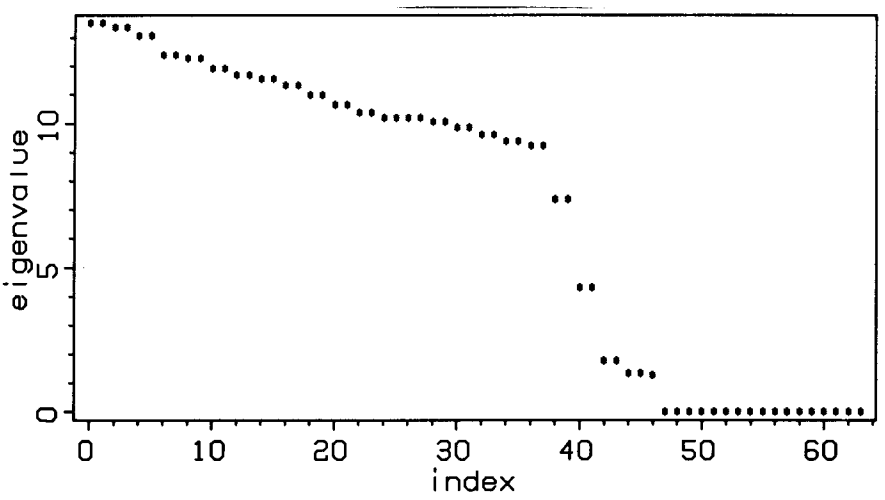

FIG. 4.13. Eigenvalues in order of decreasing size.

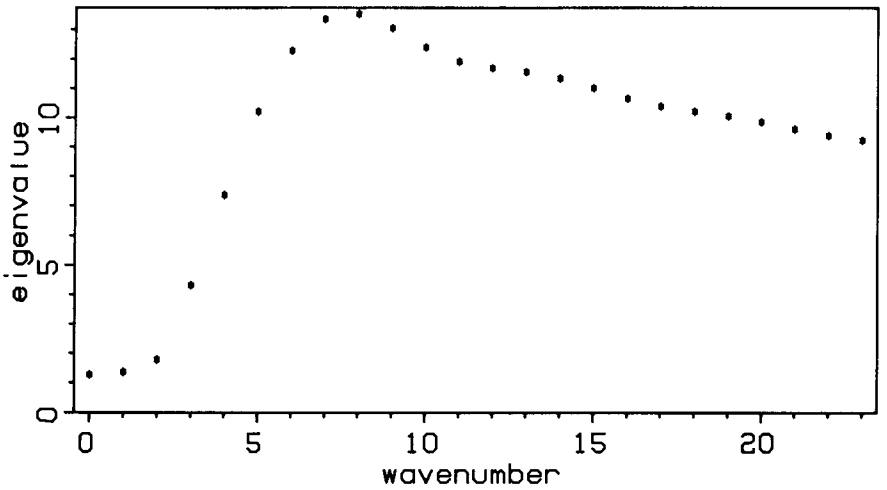

FIG. 4.14. Eigenvalue versus wavenumber of eigenvector. Note that the low wavenumber (i.e. long wavelength) components are the most poorly determined.

approximately constant within the aperture, and are thereby nearly eliminated by the operator.

These difficulties can in part be overcome if these long-wavelength components are absorbed into the background model. Incorporating lateral variations into the background distribution might seem troublesome, because the entire development assumed a constant, or at most depth-variable background-velocity. But notice that the velocity does not enter at all into the impulse response of equation (4.18). Thus the background

velocity could just as well be required to be laterally constant over an effective cable length.

A glance at the transfer function of figure 4.12 shows that there are zeroes at regular intervals, not only near the origin. Why don't these also provide problems? Because the slope of the curve is fairly steep at the later zero-crossings, a zero will appear only at certain isolated combinations of frequency, depth of anomaly and depth of reflector. Furthermore, because the zero will show up at certain combinations of wavelength and effective cable length, it will show up at different wavelengths for different depths. This is quite unlike the long-wavelength case, where the same weak response is seen at all depths.

4.6 MODEL STUDY

The nature of the linear operator relating interval slowness and stacking slowness can be more fully illustrated through a synthetic model study. The depth model shown in Figure 4.15 is adapted from Pollet (1974). The background-velocity distribution satisfies the hyperbolic moveout equation, provided that the shot to geophone offsets are not too large. The results of the model study will show that the magnitude of the anomalies—about 10%—is within the range of validity of the linearization.

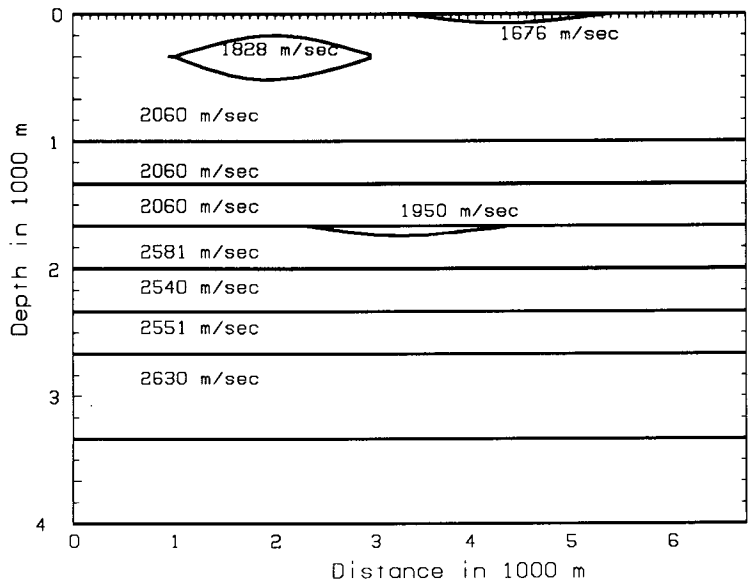

FIG. 4.15. Depth model containing three low velocity zones. Stacking velocities were determined for the reflectors at depths 1000, 1300, 2000, 2300, 2600, 3300 meters.

The first stage of the model study looks at the forward problem, that is the calculation, according to equation (4.22), of the stacking slownesses due to the interval-slowness model of figure 4.15. First, the laterally variable part of this model is expressed as a linear combination of the basis functions introduced in the previous section. Then, equation (4.22) calculates the stacking slownesses predicted by the linear theory.

These stacking slowness can then be compared to those that would be derived from the traveltimes predicted by the model. To make this comparison, traveltimes were generated with a ray-tracing program, for a standard seismic survey of 16-fold coverage (cable length = 1500 meters) over this depth model. Then, stacking slowness were determined for each of the six reflectors by fitting a line in $t^2 - x^2$ space.

Figures 4.16 and 4.17 show a comparison of the ray-trace derived stacking slownesses with the stacking slownesses derived through the linear operator, for two different background-velocity distributions. In Figure 4.16 the operator used a constant velocity background, while in Figure 4.17 it used a velocity distribution that was linear with depth. Figures 4.16 and 4.17 show that either choice of background velocity provides a very good fit with the ray-trace derived slownesses. The differences due to the differing background velocities are largest for the segments of the slowness curves most strongly influenced by the large anomaly at midpoint coordinate 1600, where the depth-variable operator clearly provides a better fit.

The linear operator modeled the anomalies of Figure 4.15 without undue error. To test the limits of validity of the linearization, I increased the magnitude of all three anomalies, by decreasing the velocity for each one by 300 m/sec. Figure 4.18 shows the same sort of comparisons as did Figures 4.16 and 4.17 (here the background velocity was taken to be depth variable). Although the basic shapes of the two sets of curves compared in Figure 4.18 are still the same (the peaks and troughs occur at the same locations), their amplitudes are clearly quite different.

In particular, the fit in the region dominated by the large anomaly at midpoint 1600 meters is much poorer than it was in any region of either Figure 4.16 or 4.17. Because the large anomaly differs in velocity from the surrounding material by an amount comparable to that of the other anomalies in the original model, the misfit must be primarily the result of the magnitude of the anomalous traveltime, rather than the anomalous velocity alone. More specifically, decreasing the velocity of the large anomaly by 300 m/sec increased its traveltime anomaly for the shallow reflector from 5% to 14%. Thus, in this case the linear approximation of the relationship between traveltime and stacking slowness was valid for a 5% traveltime anomaly, but invalid for a 14% traveltime anomaly.

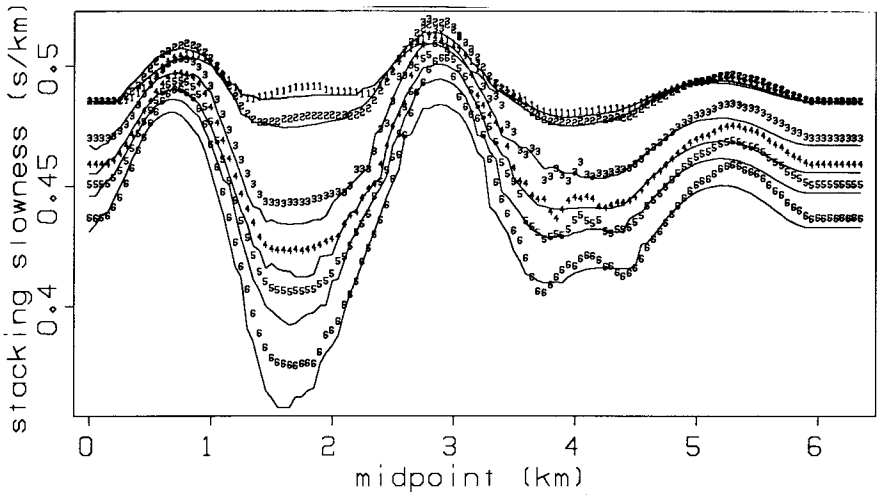

FIG. 4.16. Two sets of slowness curves determined for the six reflectors of Figure 4.15. The dotted lines represent the curves determined with the linear operator of equation (4.22), the solid lines the curves determined by fitting traveltimes from ray tracing. In this figure the forward operator used a constant background velocity.

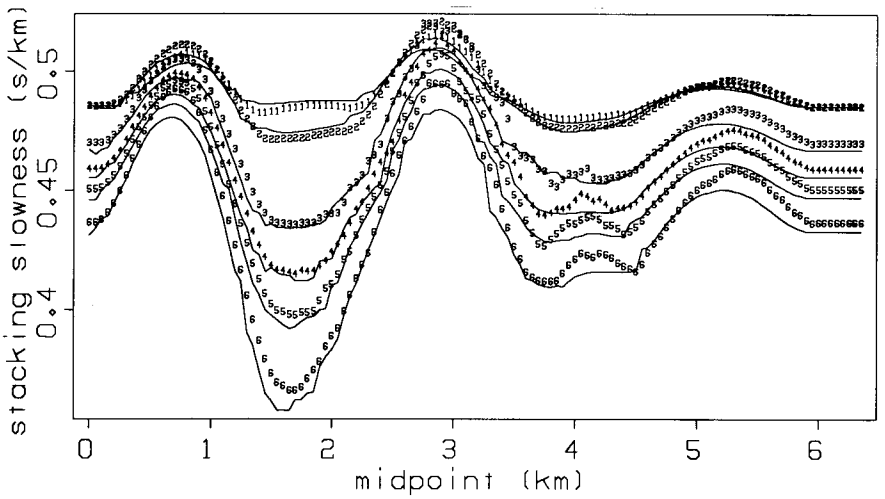

FIG. 4.17. Same as 4.16, but the forward operator used a background velocity that increased linearly with depth.

Model Study - Inversion

The next phase of this model study inverts the linear equation (4.22) connecting interval slowness and stacking slowness. For this synthetic study, I have chosen to form the generalized inverse from the matrices derived through singular value decomposition of the matrix G. Following Aki and Richards (1980), decompose **G** as follows:

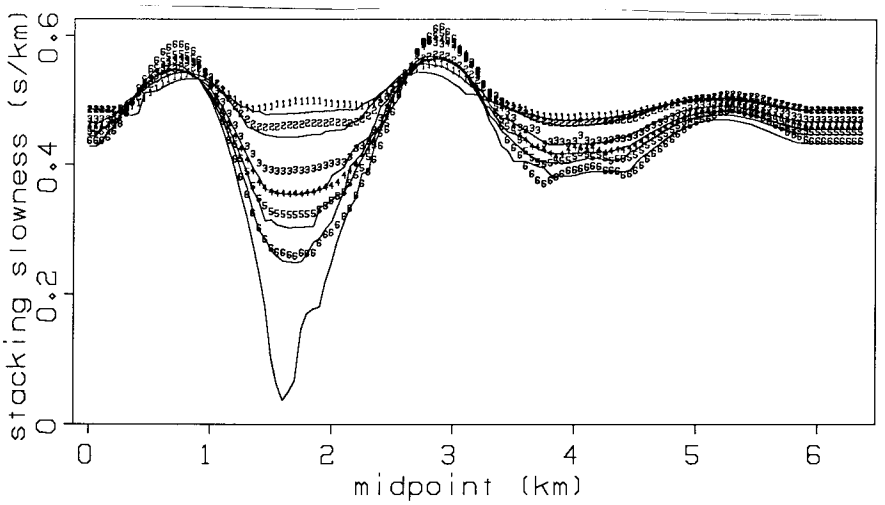

FIG. 4.18. Same as 4.17, but with all anomalous velocities decreased by 300 m/sec.

$$\mathbf{G} = (\mathbf{U}_p, \mathbf{U}_0) \begin{pmatrix} \mathbf{\Lambda}_p & 0 \\ 0 & 0 \end{pmatrix} \begin{pmatrix} \tilde{\mathbf{V}}_p \\ \tilde{\mathbf{V}}_0 \end{pmatrix}, \tag{4.25}$$

where $\mathbf{U}$ and $\mathbf{V}$ are the eigenvectors of the data and model spaces respectively, $\tilde{\mathbf{V}}$ signifies the transpose of $\mathbf{V}$, and $\mathbf{\Lambda}_p$ is a diagonal matrix of nonzero eigenvalues. $\mathbf{U}_0$ is the source of the discrepancy between the observed data and the prediction by the operator $\mathbf{G}$, while $\mathbf{V}_0$ is the source of the nonuniqueness in determining the model from the data. The generalized inverse is then

$$\mathbf{G}_g^{-1} = \mathbf{V}_p \, \mathbf{\Lambda}_p^{-1} \, \tilde{\mathbf{U}}_p \ . \tag{4.26}$$

By limiting the magnitude of the values of $\mathbf{\Lambda}_p^{-1}$, one can suppress the contributions of eigenvectors with eigenvalue less than a given value.

The first inversion example uses the ray-trace derived stacking slownesses for the original survey (with a cable length, L, of 1600 m). For easy reference, the depth model is repeated in Figure 4.19. Note once again that the stacking slownesses came from the reflectors at depths 1000, 1300, 2000, 2300, 2600, and 3300 meters. In this, and all of the subsequent inversion examples, the model consisted of 40 anomalous layers. The entire system is thus an underdetermined one (more unknowns than knowns). The largest wavenumber used corresponded to a spatial wavelength of about 300 meters; to avoid truncation artifacts, the cutoff in wavenumber was tapered.

Figures 4.20a and 4.20b are two views of the anomalous interval slownesses resulting from the inversion. The main features of the inversion are quite evident in either view: all three anomalies have been correctly found to have positive slowness (i.e. negative velocity anomalies), and have been properly positioned. While the anomalies are quite well resolved in the lateral direction, they seem to be smeared out in depth between the nearest reflectors.

This smearing is particularly evident for the deepest anomaly. In the original depth model it was 100 meters thick, at a depth of about 1650 meters; in the inverted depth model it is bounded sharply at 1300 and 2000 meters, which are the depths of the nearest reflectors used in the inversion. For the shallower anomalies the depth resolution is not completely determined by the location of the nearest reflectors, although the influence of the shallowest reflector (at depth 1000 feet) is quite evident in Figure 4.20b.

The total cable length L is a very important parameter in this stacking slowness inversion method. Loinger (1983) discussed in detail its implications for the forward problem, the most important being that the anomalous stacking-slowness response decreases in amplitude and becomes smoother as the cable length increases. Increasing the cable length also has important implications for the depth resolution in the inverse problem.

To study these effects, I once again generated traveltimes by ray-tracing through the depth model of Figure 4.19, this time with a cable length of 3200 meters (twice the previous value). Figure 4.21 shows the results of inverting the corresponding stacking slownesses. The basic features are much the same as those found with the short cable: all three anomalies have been correctly found to have positive slowness and are properly positioned. The diagonal lines (seen particularly well in the contour plot of Figure 4.21b), however, were not evident in the short cable examples, nor was the large shallow anomaly near midpoint 1650 meters as clearly resolved in depth as it is here.

A particularly striking feature of figure 4.21 is the "v" pattern, which outlines the bottom of the large shallow anomaly at midpoint 1650 meters. This effect quite clearly arises from the existence of raypaths which entirely undershoot the anomaly. Because such raypaths sense no anomalous material, they provide a boundary to the region which contains the anomaly.

The effect is further clarified by a reexamination of the results of the short cable experiment (figure 4.20). There the cable is simply too short to allow any undershooting of the anomaly, thus the absence of the clear "v" pattern. The only resolution of the lower limit of the anomaly comes from the raypaths which have, for example, the downgoing leg traveling diagonally under the anomaly, but then the upgoing leg necessarily

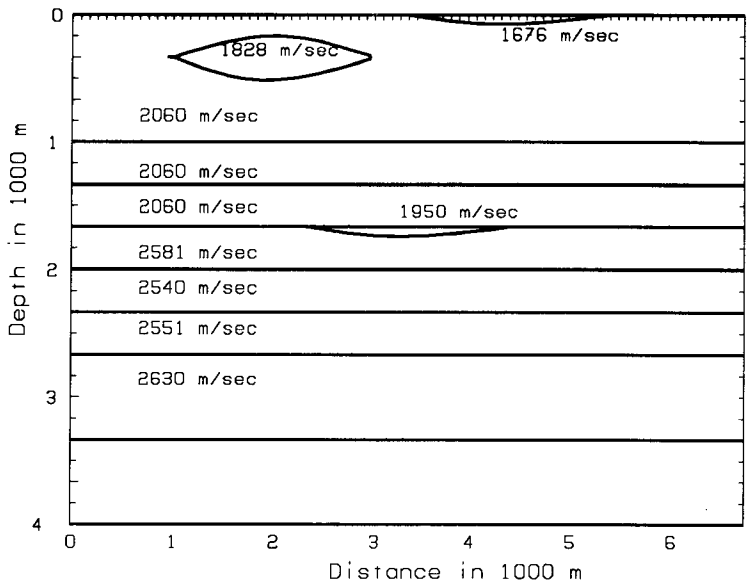

FIG. 4.19. Depth model containing three low velocity zones. Stacking velocities were determined for the reflectors at depths 1000, 1300, 2000, 2300, 2600, 3300 meters.

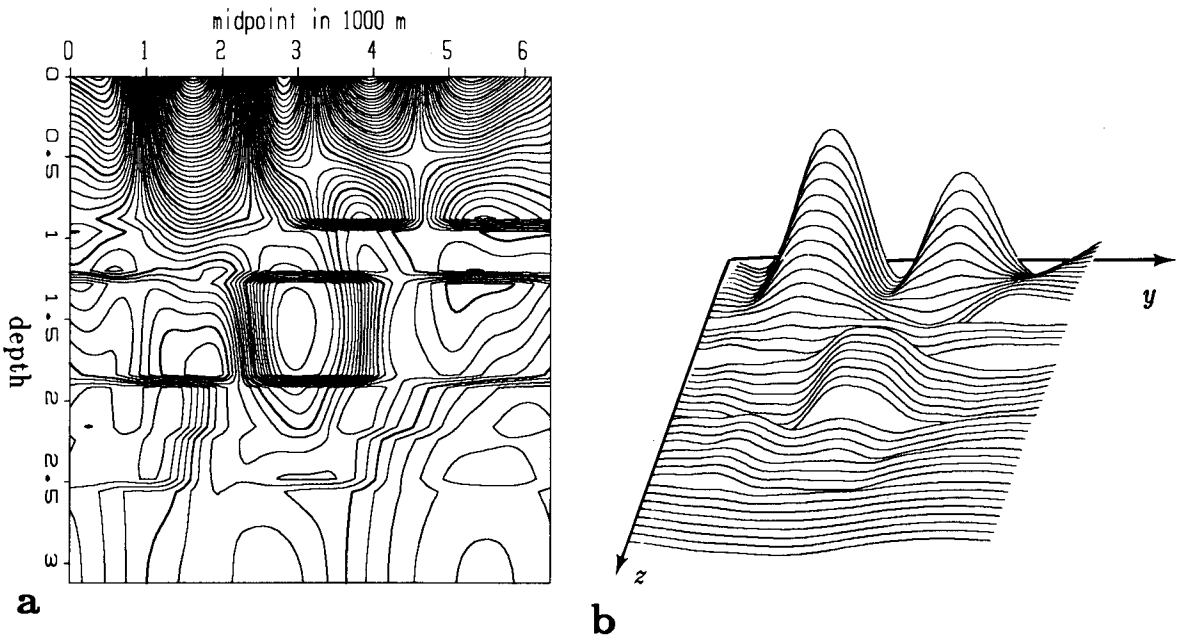

FIG. 4.20. Anomalous interval slownesses, resulting from the inversion of ray-trace derived stacking slownesses (cable length = 1600 meters). a) Contour plot. b) Hidden line drawing.

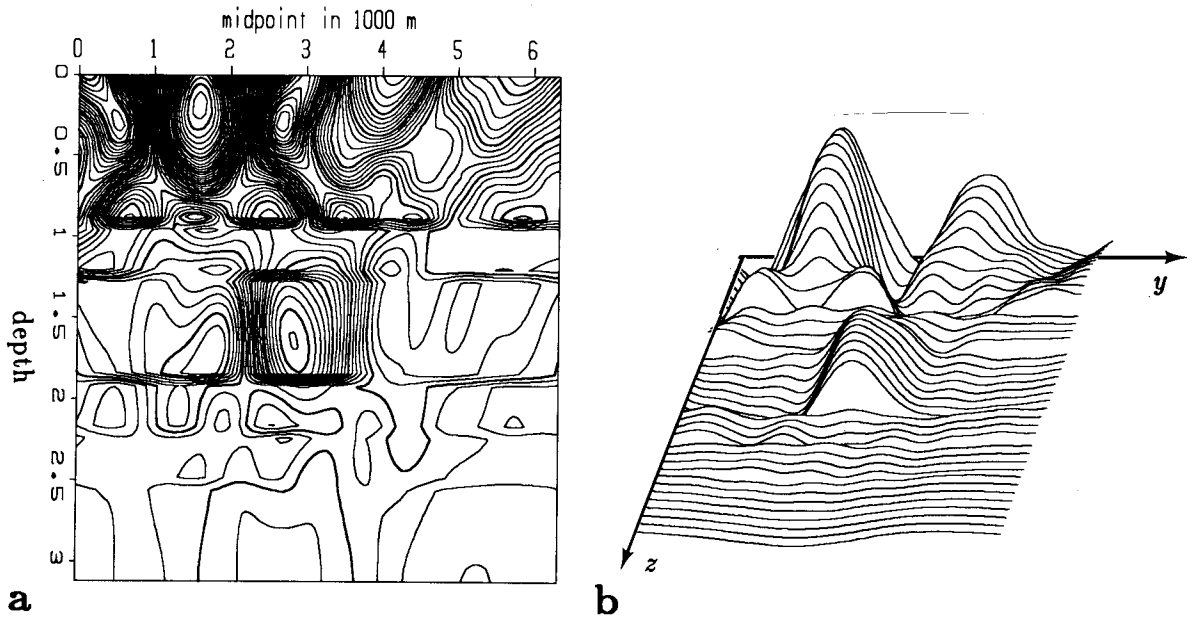

FIG. 4.21. Anomalous interval slownesses, for cable length = 3200 meters. a) Contour plot. b) Hidden line drawing.

traveling through the anomaly. The net result is that the bottom of the anomaly gets bounded by a more steeply dipping and less sharply defined line.

A similar story applies to the resolution of the top of this large shallow anomaly. For the long cable case (Figure 4.21) there are raypaths which travel entirely above the top of the anomaly. Thus, precisely as for the bottom of the anomaly, these raypaths will have sampled no anomalous material, the net effect being improved resolution of the top of the anomaly.

For the short cable case (Figure 4.20), there is no such constraint on the top of the anomaly. Indeed, a glance at the original depth model (Figure 4.19), shows that the anomaly is so shallow and broad that there is a region, for the short cable case, that is not sampled by any raypaths which do not also pass through the anomaly. The resulting effects are quite easily seen in Figure 4.20: the anomaly has a central region which is bounded above only by the surface.

The same raypath considerations apply equally well to the other two anomalies. For either choice of cable length, the basic shape of the deep anomaly is the same: the anomaly has nearly vertical side-boundaries, and is bounded above and below by the reflectors at 1300 and 2000 meters respectively (recall that the reflector at depth 1650 meters was not used). Neither of the cables is long enough to provide raypaths that

deviate far from vertical for a reflector at this depth. This results in the nearly vertical sides of the derived anomaly.

4.7 CONCLUSIONS FROM MODEL STUDY

A persistent feature of the inversion results is the large amount of low-frequency interval slowness at depth. As was explained in the section on eigenvectors and eigenfunctions, these deep low-frequency components are the most poorly determined part of the model. Their magnitude can be diminished by increasing the damping; unfortunately, this also diminishes the magnitude of the deep anomaly. Thus, there is still some doubt of how well the details of a deep anomaly can be resolved from stacking slownesses.

On the other hand, the shallow anomalies are well determined by stacking slownesses. A reason for this is that the shallow part of the model is seen by raypaths from all reflectors. Each such reflector provides a different effective cable length, and thus different aperture of the filter, for a given depth of anomaly. Thus a component of the anomaly that is poorly determined for one reflector will be well determined by a different reflector.

The results of this model study show that considerable information about laterally variable interval slownesses can be derived from stacking slownesses. Because the stacking slowness contains a combination of the information from several raypaths, the discussion emphasized that the features of the derived interval-slowness models could be explained by individual raypaths. In particular, these raypath considerations were able to explain the limited vertical resolution in the inversion results. Thus, even though the stacking slowness perturbations are a filtered version of the traveltime perturbations, the effects of this second filter can be successfully removed.

4.8 DIPPING REFLECTOR

The development so far has been based on the assumption of flat reflectors. This section extends the linear theory to the case of dipping reflectors and a constant background slowness. The starting point for the development is equation (4.4), which expresses the stacking slowness perturbation as a weighted sum of the traveltime perturbations. The derivation of this equation required no assumptions about the background model, and thus is a suitable starting point for this development. First, rewrite equation (4.4) to explicitly include all of the data and model coordinates.

$$\Delta w_s(y, z_r) = \frac{\sum_{j=1}^{n}\left(x_j{}^2 - \frac{L^2}{3}\right)}{\frac{4}{45}nL^4} \frac{t(y, z_r, x_j)}{w_s(y, z_r)} \Delta t(y, z_r, x_j) . \qquad (4.27)$$

The traveltime perturbation due to an interval-slowness perturbation is given by equation (4.6), as

$$\Delta t\,(y\,,\,z_r\,,\,x_j\,) \;=\; \int\limits_{S_j} \Delta w_{in}\,(y_a\,,\,z_a\,)\;dS_j\;. \tag{4.6}$$

Once again, S_j is the j^{th} raypath through the background model.

Figure 4.22 shows the raypath to a reflector with dip α, from the midpoint y and offset x. The half offset h, ($=\; x/2$), is also defined in figure 4.22. The depth to the reflector $z_r\,(y\,)$ is defined to be the depth of the zero-offset reflection point for the midpoint y. μ_1 and μ_2 describe the raypath: they specify the distance to the ray from the midpoint y, when the ray is at depth z_a. Naturally there are two such variables, one for each leg of the raypath.

The integral along the raypath of equation (4.6) can be reexpressed as an integral over the model, with the help of a delta function that rides along the ray. That is,

$$\Delta t_j \;=\; \Delta t\,(y\,,\,z_r\,,\,x\,) \tag{4.28}$$

$$\times \int\limits_{z_a}\int\limits_{y_a} \left[\frac{\delta(y-y_a-\mu_1(y\,,\,z_r\,,\,x_j\,,\,z_a\,),\,z_a\,)}{\cos\theta_1(y\,,\,z_r\,,\,x_j\,,\,z_a\,)} + \frac{\delta(y-y_a-\mu_2(y\,,\,z_r\,,\,x_j\,,\,z_a\,),\,z_a\,)}{\cos\theta_2(y\,,\,z_r\,,\,x_j\,,\,z_a\,)}\right] dz_a$$

Lengthy geometric analysis of figure 4.22 leads to the following expressions for μ_1 and μ_2:

$$\mu_1(y\,,\,z_r\,(y\,),\,x_j\,,\,z_a\,) \;=\; -h - z_a \left[\frac{-h\,\cos^2\!\alpha + z_r\,(y\,)\tan\alpha}{z_r\,(y\,) + h\sin\alpha\cos\alpha}\right] \tag{4.29a}$$

$$\mu_2(y\,,\,z_r\,(y\,),\,x_j\,,\,z_a\,) \;=\; h - z_a \left[\frac{h\,\cos^2\!\alpha + z_r\,(y\,)\tan\alpha}{z_r\,(y\,) - h\sin\alpha\cos\alpha}\right] \tag{4.29b}$$

Similar analysis leads to expressions for $\cos\,\theta_1$ and $\cos\,\theta_2$:

$$\cos\,\theta_1(y\,,\,z_r\,(y\,),\,x_j\,,\,z_a\,) \;=\; \frac{z_r\,(y\,)\cos\alpha + h\sin\alpha\cos^2\!\alpha}{\left(z_r^{\,2}(y\,) + h^{\,2}\cos^4\!\alpha\right)^{1/2}} \tag{4.29c}$$

$$\cos\,\theta_2(y\,,\,z_r\,(y\,),\,x_j\,,\,z_a\,) \;=\; \frac{z_r\,(y\,)\cos\alpha - h\sin\alpha\cos^2\!\alpha}{\left(z_r^{\,2}(y\,) + h^{\,2}\cos^4\!\alpha\right)^{1/2}} \tag{4.29d}$$

Furthermore, the traveltimes through the background medium obey the NMO equation, provided that a cosine-corrected slowness is used (Levin, 1971).

$$t_j \;=\; t\,(y\,,\,z_r\,(y\,),\,x_j\,) \;=\; w\cos\alpha\,\left(x_j^{\,2} + 4z_r^{\,2}(y\,)\right)^{\frac{1}{2}} \tag{4.30}$$

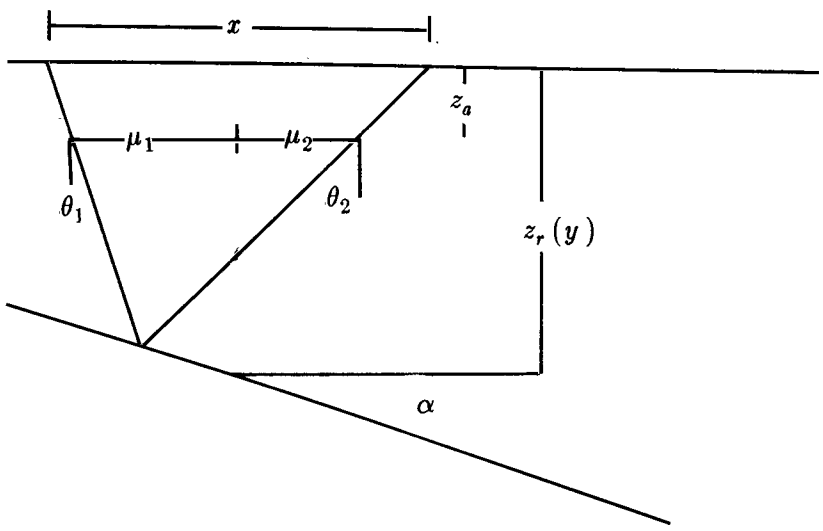

FIG. 4.22. Raypath to a reflector with dip α, from the midpoint y and offset x. $z_r(y)$ is the depth of the zero-offset reflection point for the midpoint y.

Equations 4.29 and 4.30 provide analytic expressions for all of the raypath variables of equation (4.27). Thus, by analogy with the flat reflector case, the integral over offset would select from the integral the offset of the ray that went through the point (y_a, z_a) for this reflector and midpoint gather. The information of which offset has its ray going through the point (y_a, z_a) is provided by the argument of the delta function.

Unfortunately, when the reflector has non-zero dip, the rays from more than one offset may go through the point (y_a, z_a). Figure 4.23 shows how this can happen: it is a consequence of the well-known reflection-point dispersal for a dipping reflector. As the offsets get progressively wider, the reflection point moves progressively up-dip, and thus the raypaths within the CMP gather must cross. A formal statement of this is that the derivative of equation (4.29b) with respect to offset is zero for some offset.

If the offset is sufficiently small, the area of raypath crossing will be insignificant. The impulse response can then be constructed if the stacking slowness is assumed to be insensitive to the values of interval slowness immediately above the reflector. These difficulties can also be bypassed with a numerical approach: instead of analytically calculating the impulse response, derive the matrix that relates perturbations in a discrete model to the resulting perturbations in stacking slowness. This numerical approach is taken in the remainder of this section.

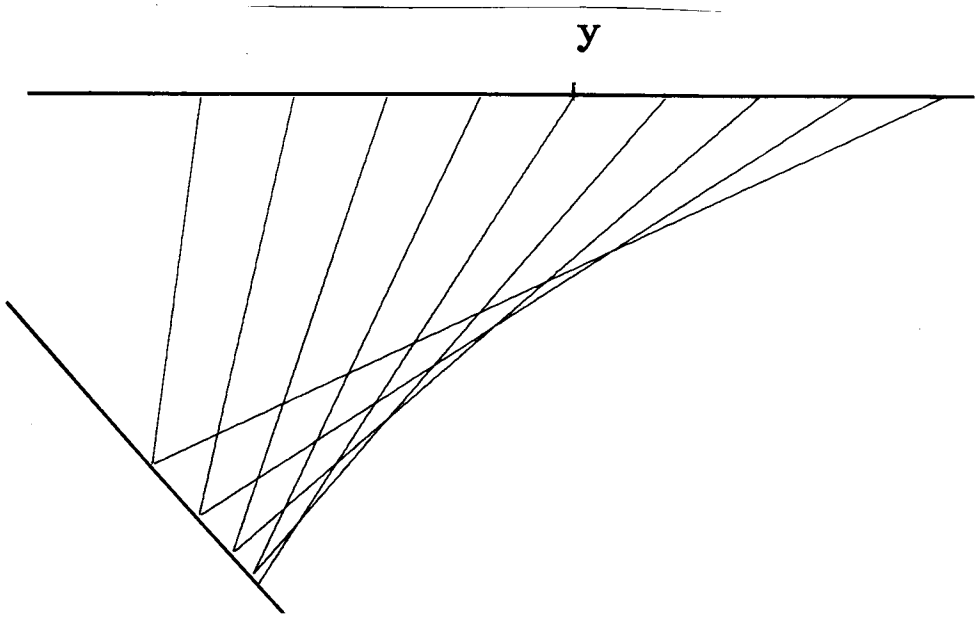

FIG. 4.23. Raypaths for several offsets to a dipping reflector. Note that a consequence of the reflection-point dispersal is the crossing of the raypaths for this midpoint gather.

Consider then, a discrete model with basis functions that are small rectangular regions. Then, the matrix **G**, relating perturbations in this model to stacking slowness, can be constructed. The matrix can be most easily be constructed one row at a time, that is for one midpoint and reflector. For each offset, the raypath for this particular midpoint and reflector can be traced through the model. Whenever this raypath passes through the region corresponding to a model parameter, the appropriate column of the matrix has its entry for the given row increased by the offset-dependent weight. This construction of the matrix **G** is quite similar to what is commonly done in seismic tomography (Aki and Richards, 1980); the difference is in the offset-dependent weights due to the use of stacking slownesses.

Figure 4.24 shows how the different parts of an interval slowness model affect the stacking slowness for one dipping reflector, at one midpoint. That is, it shows one row of the matrix. The obvious feature is that the "fan" is now skewed. The large amplitude response at the model points where rays cross is also visible in Figure 4.24.

This section has discussed the stacking slowness response for a dipping reflector, to an anomalous interval-slowness distribution. The analytic determination of the impulse response is complicated by the crossing of rays within a CMP gather. On the other hand, the dipping reflector can be handled by a numerical approach, based on a discrete model of interval slowness. This numerical approach, which was taken in the construction of Figure 4.24, is a very general one that could also be applied to other, more

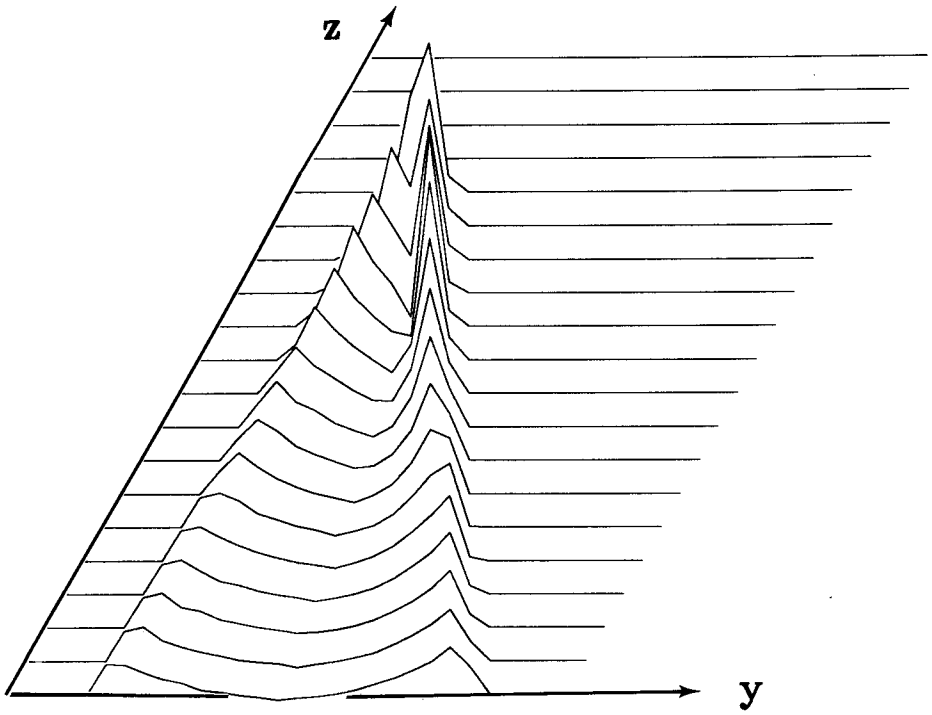

FIG. 4.24. This figure shows how the different parts of an interval slowness model affect the stacking slowness for one dipping reflector, at one midpoint. That is, it shows one row of the matrix relating perturbations in a discrete interval slowness model to perturbations in stacking slowness.

complicated background models.